RESEARCH ARTICLE

CATALYSIS

Cooperative adsorbate binding catalyzes high-temperature hydrogen oxidation on palladium

Michael Schwarzer[1,2], Dmitriy Borodin[1,2]†, Yingqi Wang[3], Jan Fingerhut[1], Theofanis N. Kitsopoulos[2,4], Daniel J. Auerbach[2], Hua Guo[3], Alec M. Wodtke[1,2,5]*

Atomic-scale structures that account for the acceleration of reactivity by heterogeneous catalysts often form only under reaction conditions of high temperatures and pressures, making them impossible to observe with low-temperature, ultra-high-vacuum methods. We present velocity-resolved kinetics measurements for catalytic hydrogen oxidation on palladium over a wide range of surface concentrations and at high temperatures. The rates exhibit a complex dependence on oxygen coverage and step density, which can be quantitatively explained by a density functional and transition-state theory–based kinetic model involving a cooperatively stabilized configuration of at least three oxygen atoms at steps. Here, two oxygen atoms recruit a third oxygen atom to a nearby binding site to produce an active configuration that is far more reactive than isolated oxygen atoms. Thus, hydrogen oxidation on palladium provides a clear example of how reactivity can be enhanced on a working catalyst.

Since the early 1800s, when Döbereiner first amazed the public and fellow natural philosophers by oxidizing hydrogen over a platinum sponge to create "fire without flint and tinder" (1, 2), heterogeneous catalysis has revolutionized chemistry. Platinum-group metal catalysts in particular have proven to be some of the most important materials in modern industry (3). Applications include the catalytic removal of pollutants from combustion (4, 5), hydrogen production and purification (6, 7), catalytic fuel cells (8–10), chemical catalysis (11–13), and the production of artificial fertilizers (14, 15). Despite its importance, we still lack a mechanistic understanding of most reactions in heterogeneous catalysis.

To appreciate the challenges involved, consider that gas-phase reactivity occurs within a homogeneous environment and depends only on the relative positions and velocities of the reacting atoms. However, in heterogeneous catalysis, reactivity also depends on the positions of the reactants with respect to a catalytic surface. For example, even on single crystal surfaces, the most homogeneous catalysts one can produce in the laboratory, reactions often occur selectively at a tiny minority of step "defect" sites where low-valence metal atoms are present (16, 17). The concept of active sites has thus become central to our thinking about surface chemistry, and they can sometimes be identified on pristine crystalline surfaces using low-temperature microscopy (18).

Unfortunately, there is no general way to determine the nature of active sites at the high temperatures and pressures typical of real catalysis. There is also evidence that barrier heights and the energies of reaction intermediates can be influenced by so-called spectator adsorbates (19, 20). Adding to the challenge, real catalytic surfaces operating at high temperatures and pressures are hardly pristine and may exhibit reactive structures, what we call active configurations, that may not even exist under nonreactive conditions. Therefore, determining the properties of active configurations present on dynamic catalysts (21–24) operating under reacting conditions is an important challenge in modern surface chemistry (25).

We report high-precision velocity-resolved kinetics (26, 27) measurements over a wide range of coverages and temperatures, as well as results from theoretical kinetics involving density functional theory (DFT) and transition-state theory (TST), which reveal the mechanism of hydrogen oxidation on Pd catalysts. The reaction involves an active configuration of cooperatively-bound oxygen atoms that forms along a Pd step only under conditions with elevated oxygen concentrations. At reduced oxygen concentrations, the reaction slows dramatically and the kinetic order changes. These results show how reactivity can be enhanced on a working catalyst operating under reacting conditions.
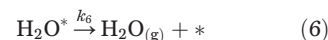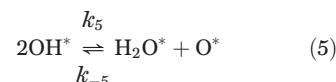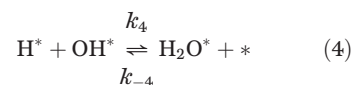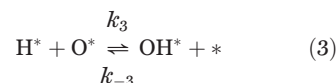
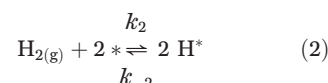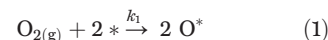### Background

We outline what was known about the kinetics of this reaction before this study.

The overall reaction can be formally written as

$$O_{2(g)} + 2H_{2(g)} \xrightarrow{Pd} 2H_2O_{(g)}$$

where activated forms of $H_{2(g)}$ and $O_{2(g)}$ are first produced by dissociative adsorption. Subsequently, the adsorbates (indicated by an asterisk) recombine to form thermodynamically stable water (28–30). Only a few elementary reactions are possible.

$$O_{2(g)} + 2* \xrightarrow{k_1} 2\,O^* \qquad (1)$$

$$H_{2(g)} + 2* \underset{k_{-2}}{\overset{k_2}{\rightleftharpoons}} 2\,H^* \qquad (2)$$

$$H^* + O^* \underset{k_{-3}}{\overset{k_3}{\rightleftharpoons}} OH^* + * \qquad (3)$$

$$H^* + OH^* \underset{k_{-4}}{\overset{k_4}{\rightleftharpoons}} H_2O^* + * \qquad (4)$$

$$2OH^* \underset{k_{-5}}{\overset{k_5}{\rightleftharpoons}} H_2O^* + O^* \qquad (5)$$

$$H_2O^* \xrightarrow{k_6} H_2O_{(g)} + * \qquad (6)$$

All prior studies suggest that reaction (3) is rate-limiting. However, the derived activation energies differ widely from one another (0.3 to 0.8 eV) (31–33). A comparison with electronic structure calculations, which predict a barrier to OH^* formation of ~1 eV and that reaction (5) is barrierless on a defect-free Pd(111) surface (34, 35), suggests that the rate of reaction may depend strongly on details of the experimental conditions, such as the step density of the catalyst. Beyond this, the relative importance of reactions (4) and (5) has remained unknown (31, 33, 36).

Experimental results

Figure 1 shows representative water formation rates (left panels) obtained with velocity-resolved kinetics; here, two pulsed molecular beams and a leak valve were available for pulsed and continuous reactant deposition, and a high-power, short-pulsed laser was used for nonresonant multiphoton ionization of desorbed products. Ion-imaging provided velocity-resolved product detection (26, 27). See the supplementary materials, section S1, for additional experimental details. Results are presented under oxygen-rich (Fig. 1, A to C) and oxygen-lean (Fig. 1, D to F) conditions and for low- and high-Pd step densities. The reaction was unexpectedly complex. For oxygen-rich conditions, it proceeded much faster on a surface with high step density (Fig. 1A), whereas for oxygen-lean conditions (Fig. 1D), the reaction was much slower and depended only weakly on step

[1]Institute for Physical Chemistry, University of Göttingen, 37077 Göttingen, Germany. [2]Department of Dynamics at Surfaces, Max Planck Institute for Multidisciplinary Sciences, 37077 Göttingen, Germany. [3]Department of Chemistry and Chemical Biology, Center for Computational Chemistry, University of New Mexico, Albuquerque, NM 87131, USA. [4]School of Mathematics and Natural Sciences, University of Southern Mississippi, Hattiesburg, MS 39406, USA. [5]International Center for Advanced Studies of Energy Conversion, 37077 Göttingen, Germany.
*Corresponding author. Email: alec.wodtke@mpinat.mpg.de
†Present address: Center for Quantum Nanoscience, Ewhayeodae-gil 52, Daehyeon-dong, Seodaemun-gu, Seoul 03760, South Korea.
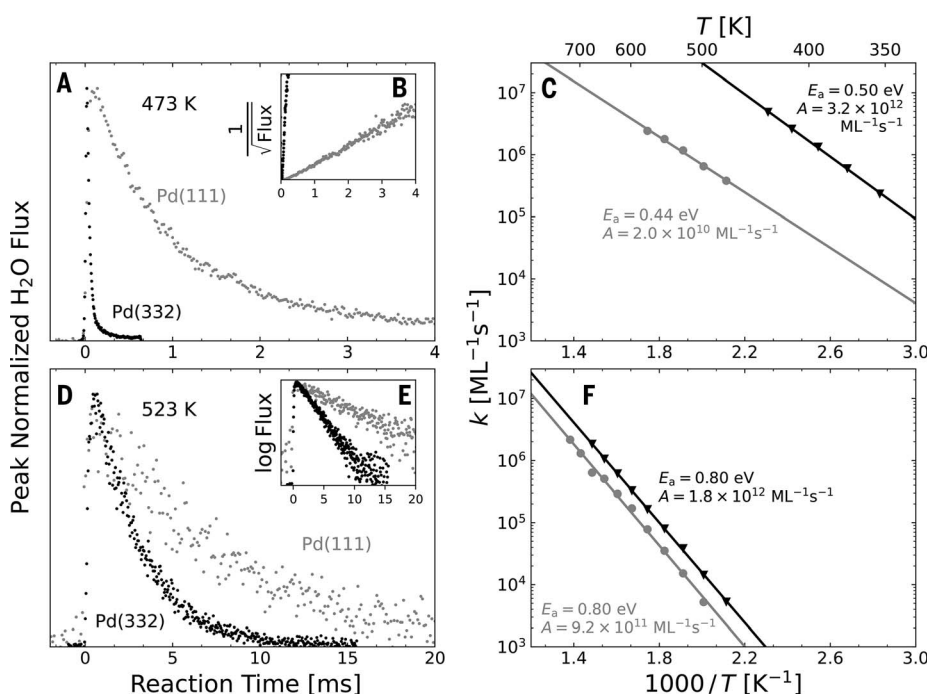
Fig. 1. The kinetics of catalytic hydrogen oxidation on Pd: Dependence on oxygen coverage, step density, and temperature. (**A**) Experimentally observed water formation rates for Pd (332) (black dots) and (111) (gray dots) at 473 K for $[O^*_{mean}] = 0.03$ ML. We define 1 ML as the coverage corresponding to a one-to-one ratio of adsorbate molecules to Pd surface atoms. The H-atom coverage $[H^*]$ is limited by the dose (0.002 ML) of the reaction-initiating H_2 pulsed beam. (**B**) Second-order linearization of the rate data (see also fig. S3). (**C**) Arrhenius plots of the rate constants obtained from data as shown in (A). (**D**) Same as (A) but $[H^*] = 0.008$ ML and the $[O^*_{mean}]$ is limited by the dose (0.001 ML) of the reaction-initiating O_2 pulsed beam. (**E**) First-order linearization of the rate data. (**F**) Arrhenius plots of the rate constants obtained from data of (D).
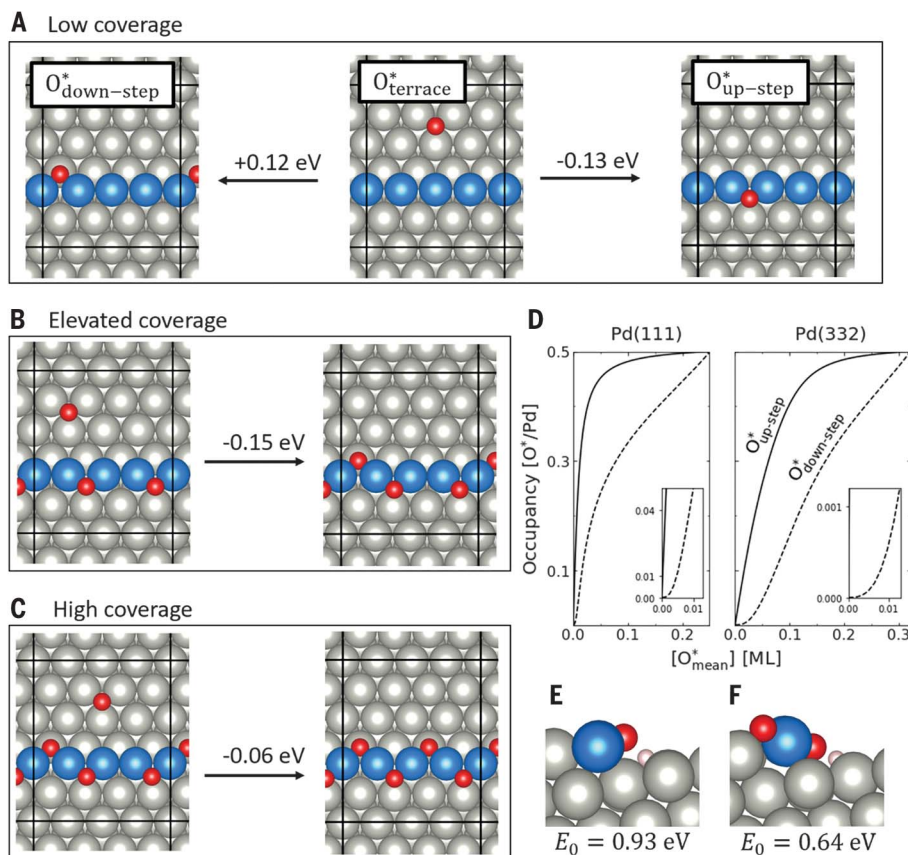
Fig. 2. Theoretical predictions of cooperative binding of O* on the stepped Pd(332) surface. (**A**) In the isolated-atom limit, $O^*_{up-step}$ is bound most strongly. (**B**) At higher oxygen coverage, the $O^*_{up-step}$ occupation rises, increasing the probability to find $O^*_{up-step}$ neighbors, which stabilize the binding of $O^*_{down-step}$. (**C**) The cooperative stabilization energy is reduced as the steps become saturated. The black lines show the unit cell defining the periodic boundary conditions used in the DFT calculations. (**D**) Equilibrium populations of $O^*_{up-step}$ and $O^*_{down-step}$ versus mean $[O^*]$ for Pd (332) and (111) at 473 K. The step densities of the (111) and (332) surfaces are 0.2 and 16.7%, respectively. (**E** and **F**) Transition state of OH* formation at $O^*_{up-step}$ (E) and at $O^*_{down-step}$ (F). Terrace Pd atoms are shown in gray, step Pd atoms in blue, O atoms in red, and H atoms in pink. Calculations were done using RPBE.

density. Even the order of the reaction kinetics changed. Second-order reactions were seen under oxygen-rich conditions (Fig. 1B), whereas pseudo–first-order kinetics were seen for oxygen-lean conditions (Fig. 1E). Based on these obser-

vations, second-order reaction rate constants were derived from basic kinetics assumptions (Fig. 1, C and F). For oxygen-rich conditions, in which a pulse of H_2 impinges onto an O-covered surface, we assumed that all H_2

molecules from the molecular beam undergo an A+A type second-order reaction to yield the observed transient shape (see the supplementary materials, section S2 for more details). For oxygen-lean conditions, in which a pulse of O_2
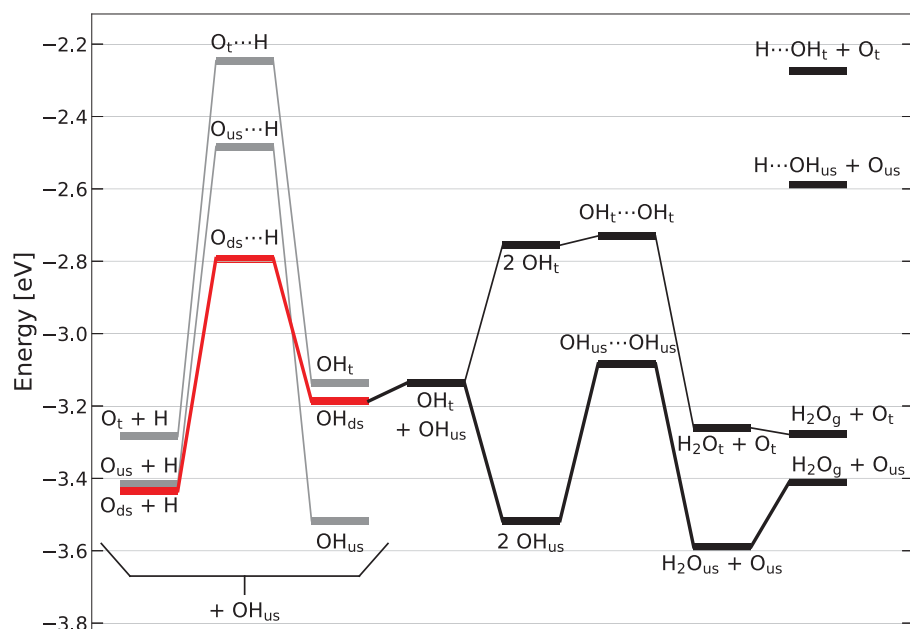
Fig. 3. Reaction paths involved in the Pd-catalyzed conversion of hydrogen and oxygen to water. The dominant reaction flux on Pd(332) at elevated O coverages (red) involves OH* formation at the $O^*_{down-step}$ site, diffusion of OH* to terraces and subsequent trapping at steps, followed by disproportionation to form water. At low O* coverages, OH* is formed at the $O^*_{up-step}$ site. The energy of an additional $OH^*_{up-step}$ adsorbate molecule has been added to all energies along the OH* formation pathway to ensure mass balance in the subsequent disproportionation reaction. See fig. S9 for more details. For comparison, the transition-state energies for the OH* + H* reaction are also shown. All structures used to construct this diagram can be found in tables S5 to S7. These results were obtained with the RPBE functional; similar results for the PBE functional can be found in the supplementary materials. The zero of energy refers to gas phase reactants and all energies are ZPE corrected. Note that down-step, up-step, and terrace are abbreviated ds, us, and t, respectively.

impinges on an H-covered surface, we applied pseudo–first-order conditions for the H-atom coverage to obtain reaction rate constants. See section S3 of the supplementary materials for additional details.

Comparison with DFT results

These observations suggested that the rate-limiting reaction changed with oxygen coverage. For oxygen-rich conditions (Fig. 1C), the experimentally derived activation energies of 0.44 ± 0.02 eV on Pd(111) and 0.50 ± 0.01 eV on Pd(332) compared well with our DFT-computed barrier heights using two functionals (RPBE: 0.43 eV, PBE: 0.40 eV) for the OH* disproportionation, reaction (5), occurring at steps (table S8). This result also explained the second-order kinetics.

For oxygen-lean conditions, the experimentally derived activation energies of 0.80 ± 0.01 eV on Pd(111) and 0.80 ± 0.01 eV on Pd(332) were similar to DFT predicted barrier heights (RPBE: 0.93 eV, PBE: 0.93 eV) for OH* formation at steps, a reaction that we expected to exhibit pseudo–first-order kinetics under our experimental conditions. We concluded that the rate-limiting step for water formation under oxygen-lean conditions was OH* formation

occurring at steps, whereas OH* disproportionation occurring at steps was rate-limiting under oxygen-rich conditions.

The fact that the rate-limiting step changed suggested that the barrier to OH* formation dropped with increasing oxygen coverage, an effect that is inconsistent with the behavior of isolated O atoms. Figure 2 shows results of DFT calculations performed on a 4×1 unit cell with periodic boundary conditions (computational details are presented in the supplementary materials, section S4), which provided insights into how the rate-limiting reaction could change with O coverage. Figure 2A depicts O* structures on a Pd (332) surface in the isolated-atom limit. Here, O* binds most favorably above a face-centered cubic (fcc) hollow site next to a monatomic step, hereafter referred to as $O^*_{up-step}$, and somewhat less stably at the fcc hollow sites of the (111) terrace, hereafter referred to as O^*_{terr}. Binding at the fcc face of the (111) step, hereafter referred to as $O^*_{down-step}$, was unstable with respect to O^*_{terr} or $O^*_{up-step}$. However, as can be seen in Fig. 2B, $O^*_{down-step}$ became stable in the presence of two neighboring $O^*_{up-step}$ atoms.

These cooperative interactions suggested that at increased oxygen coverage, a "zigzag" O-decorated Pd step structure (Fig. 2C) could

form, similar to one that has been previously studied (37, 38). Of great consequence to the reactivity, the barrier for OH* formation was substantially lower for reaction at $O^*_{down-step}$ (RPBE: 0.64 eV, PBE: 0.60 eV) compared with the reaction at $O^*_{up-step}$ (RPBE: 0.93 eV, PBE: 0.93 eV). We hypothesize that the OH disproportionation reaction became rate limiting under oxygen-rich conditions because the barrier to OH formation was reduced by the presence of $O^*_{down-step}$, formed through cooperative O-atom binding at Pd steps.

We next computed equilibrium populations of $O^*_{down-step}$ and $O^*_{up-step}$ as a function of $\left[O^*_{mean}\right]$ and T using the kinetic model introduced below. Figure 2D shows that the population of $O^*_{down-step}$ was important at all but the lowest mean coverages. It grew as $\left[O^*_{mean}\right]^2$ at low $\left[O^*_{mean}\right]$, because two $O^*_{up-step}$ in close proximity to one another were needed to stabilize $O^*_{down-step}$. These results showed that $O^*_{down-step}$ exhibited higher reactivity toward OH* formation and was present in sufficient abundance, which made it a candidate for the cooperatively formed active configuration hypothesized above.

Mechanism and kinetic modeling

We next present a reaction mechanism involving cooperative O-atom binding to obtain TST rate constants based on DFT energies and vibrational frequencies (see the supplementary materials, sections S4 to S8 for details). Figure 3 shows the potential energy diagram for water formation. The lowest-energy pathway from reactants to products for oxygen-lean conditions formed OH* through reaction of H* with $O^*_{up-step}$, whereas under oxygen-rich conditions, H* reacted with $O^*_{down-step}$. In both cases, newly formed OH* was strongly bound at Pd steps and could undergo disproportionation to produce H_2O.

Figure 4A (oxygen-rich) and Figure 4B (oxygen-lean) show that the TST model's predictions based on both RPBE and PBE input data were similar to experiment (for a comparison with all experimental data, see the supplementary materials, section S9). Figure 4A also shows that neglect of OH* formation at $O^*_{down-step}$ resulted in unrealistically slow water formation rates under oxygen-rich conditions. Figure 4B shows that OH* formation at $O^*_{down-step}$ was unimportant under oxygen-lean conditions. A systematic degree-of-rate-control (DRC) analysis (39, 40) of the DFT- and TST-based mechanism (see the supplementary materials, section S10) showed that under oxygen-rich conditions, water production rates were sensitive to the OH* formation rate at $O^*_{down-step}$ and the OH* disproportionation rate at step sites. Under oxygen-lean conditions, the water production rate was sensitive only to OH* formation at $O^*_{up-step}$.

This DRC analysis of the kinetic model informed us which energies in Fig. 3 most influenced the experimental kinetic traces. As
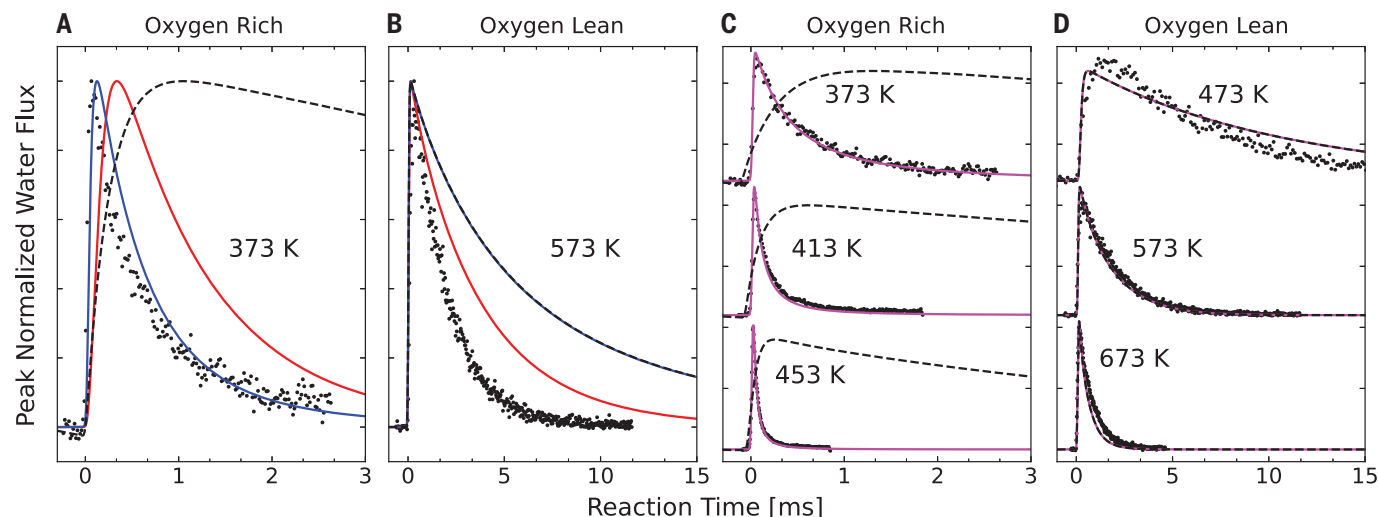
Fig. 4. Comparison of experimental and theoretical kinetic traces for water formation in hydrogen oxidation on Pd (332). Velocity-resolved kinetics results (black dots), TST microkinetic model based on RPBE (red line), PBE (blue line), and the optimized model (purple line). For PBE and the optimized model, results are also shown neglecting reactivity at the down-step O atom (dashed line). (**A**) $[O^*_{mean}] = 0.09$ ML. (**B**) $[H^*] = 0.003$ ML. (**C**) $[O^*_{mean}] = 0.09$ ML. (**D**) $[H^*] = 0.026$ ($T = 473K$), 0.003 ($T = 573K$), and 0.0007 ML ($T = 673K$). For (A) and (C), the H coverage is limited by the dose (0.002 ML) of the reaction-initiating H_2 pulsed beam. For (B) and (D), the O-atom coverage is limited by the dose (0.001 ML) of the reaction-initiating O_2 pulsed beam. We define one ML as the coverage corresponding to a one-to-one ratio of adsorbate molecules to Pd surface atoms.

shown in Fig. 4, C and D, adjusting these energies by not more than 0.15 eV led to quantitative agreement between the kinetic model and experiment under both oxygen-rich and oxygen-lean conditions. Section S11 of the supplementary materials explains the fitting procedure and shows comparisons of experimental and simulated kinetic traces of the optimized model over a wide range of coverages (10^{-4} ML $< [O^*] < 0.2$ ML) and temperatures (353 K $< T_S < 873$ K). Different adjustments were made for oxygen-lean (table S14) and oxygen-rich (table S15) conditions to account for repulsive interactions between OH^* and O^* that are neglected in the DFT energies of the kinetic model. Such interactions can be important under oxygen-rich conditions and are assumed to be absent under oxygen-lean conditions. These effects are discussed at length in the supplementary materials, section S12.

A comprehensive comparison of the optimized model to experiment over all experimental conditions is possible using effective rate constants (as explained in the supplementary materials, sections S2 and S3, and shown in Fig. 5). Under oxygen-lean conditions, the model reproduces the pseudo–first order kinetics and the linear dependence of k_{eff} on hydrogen coverage. Under oxygen-rich conditions, the peculiar dependence of the second order k_{eff} on O-atom coverage is captured by the optimized model. The maximum rate constant on Pd(332) appears at somewhat higher O coverages in the model than in the experiment. Despite these modest differences, the optimized model captures the peculiar step and O coverage dependence seen in experiment.

Discussion

This work answers basic questions concerning the elementary reactions responsible for the catalytic conversion of hydrogen and oxygen to water on Pd. It shows that at O coverages of ~10^{-3} monolayers (ML), OH^* formation was the rate-limiting step to water formation, whereas at higher coverages, the barrier to this reaction dropped and made OH^* disproportionation the rate-limiting reaction. This peculiar change in kinetic mechanism resulted from the formation of an active configuration by cooperative binding of multiple O-atoms at Pd steps. This active configuration dominated the reaction under nearly all conditions; indeed, it is remarkable that conditions where it was unimportant arose only at very low O coverages on the order of 0.001 ML.

The evidence for our conclusions came from a comparison of experimentally obtained and theoretically derived kinetics, which were in quantitative agreement with one another after DFT-computed energies along the reaction path were adjusted by up to ±0.15 eV. These adjustments are justified given uncertainties related to the use of DFT. Specifically, computed energies may vary by up to 0.2 eV depending on choice of functional (41) and the choice of unit cell size enforces specific and high adsorbate coverages. For example, the calculations of this work used to compute cooperative O-atom binding correspond to 0.125 and 0.167 ML (Fig. 2, B and C), but were used to construct a kinetic model for much lower coverages as well. A discussion of these issues is provided in the supplementary materials, section S6, where we show that low coverage calcula-

tions yield similar results for the formation of down-step O atoms. Furthermore, our model is a simplified microkinetic model with an equilibrium assumption to obtain the site-specific O-atom populations and neglects OH^* interactions with O^*. Future work, using the kinetic Monte Carlo approach would allow us to go beyond these approximations and provide an improved treatment of adsorbate-adsorbate interactions. It would also be desirable to go beyond the harmonic approximation and to include tunneling in TST calculations. Despite these limitations, our kinetic model achieved quantitative agreement with observation over a wide range of conditions. Most importantly, the kinetic model described the peculiar dependence of the observed kinetics on oxygen coverage, by means of a cooperatively bound active configuration, the abundance of which is strongly dependent on $[O^*_{mean}]$.

Our results also provided a test of DFT implemented at the generalized gradient approximation (GGA) level for calculating reaction barriers in catalysis, where few direct comparisons between experiment and theory have been possible. Although DFT-GGA involves intrinsic energy errors on the order of 0.2 eV, much larger errors can arise from an incorrect hypothesis about the structures of active configurations. In this work, finding the correct structures of the transition states of the rate limiting steps was much more important than a "correct" choice of functional. This suggests that the field may use DFT-GGA with guarded optimism, for example by developing new DFT-GGA–based discovery tools for active configurations formed due to cooperative adsorbate interactions.
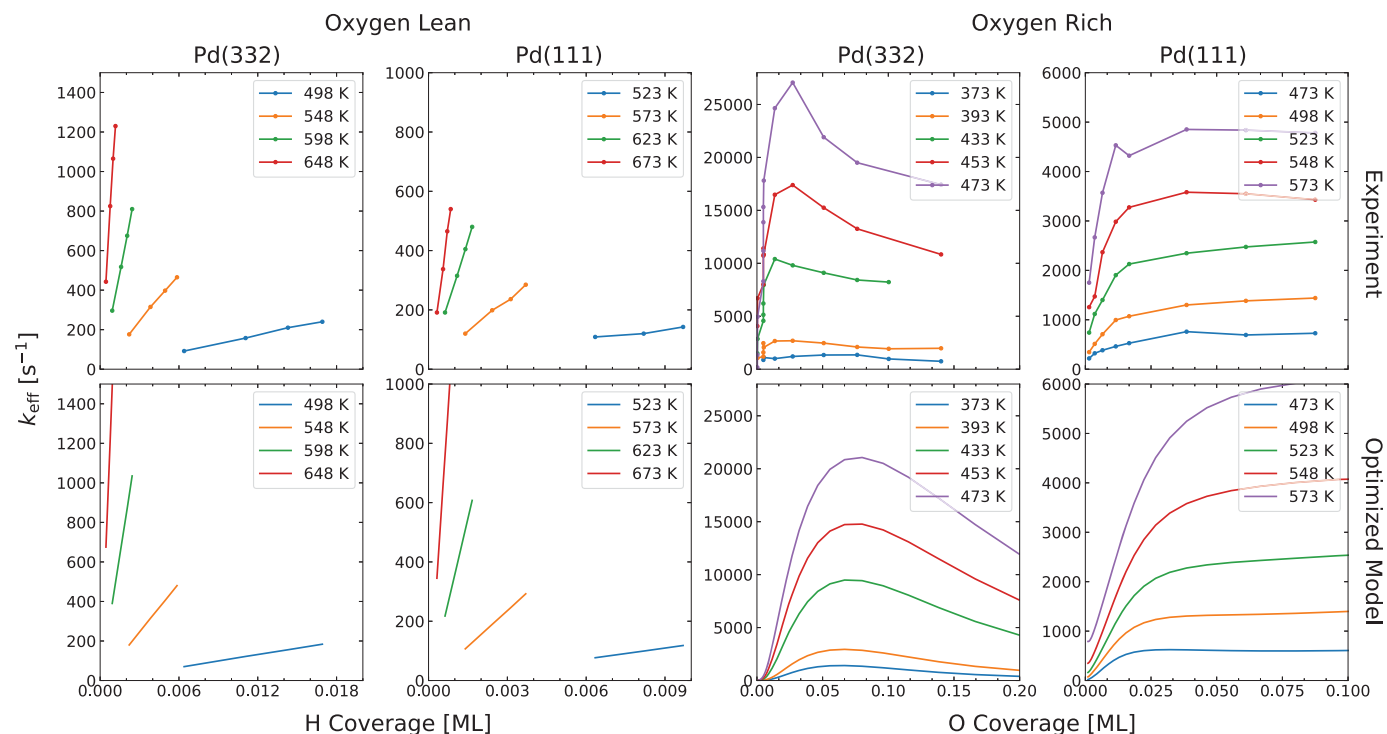
Fig. 5. Behavior of effective rate constants k_{eff} as a function of coverage (see the supplementary materials, sections S2 and S3). Shown are oxygen-lean conditions as a function of H-atom coverage (left half) and oxygen-rich conditions as a function of O-atom coverage (right half). The top row shows effective rate constants obtained from experimental traces which compare well with effective rate constants obtained from traces of the optimized kinetic model, shown in the bottom row.

Cooperative adsorbate binding is seldom discussed in heterogeneous catalysis, but it is well known in other fields such as biochemistry, in which the docking of one ligand enhances affinity for a second ligand (42, 43). Such behavior was first recognized through the nonlinear dependence of binding site occupation on ligand concentration in O_2 binding to hemoglobin (44). It should therefore not come as a surprise that active configurations formed by cooperative adsorbate binding such as the zigzag O-decorated steps are present under the reacting conditions of catalysts, and that such effects can be recognized by their nonlinear dependence on adsorbate concentration. There is also reason to believe that such active configurations are important in high-pressure, high-temperature reactors. First-principles statistical mechanics calculations of equilibrium structures have shown that O-decorated Pd step structures similar to those of this work are thermodynamically stable at high temperatures and pressures (45). We speculate that such active configurations caused by cooperative adsorbate interactions may play an essential role in many examples of real-world catalysis.

REFERENCES AND NOTES

1. J. W. Döbereiner, *Ann. Phys.* **74**, 269–273 (1823).
2. J. W. Döbereiner, *Anat. Physiol.* **1**, 989–990 (1823).
3. K. Nose, T. H. Okabe, *Treatise on Process Metallurgy* (Industrial Processes, 2014), vol. 3, pp. 1071–1097.
4. G. Busca, L. Lietti, G. Ramis, F. Berti, *Appl. Catal. B* **18**, 1–36 (1998).
5. J. Wang, H. Chen, Z. Hu, M. Yao, Y. Li, *Catal. Rev., Sci. Eng.* **57**, 79–144 (2015).
6. S. Yun, S. T. Oyama, *J. Membr. Sci.* **375**, 28–45 (2011).
7. S. N. Paglieri, J. D. Way, *Separ. Purif. Methods* **31**, 1–169 (2002).
8. M. Shao, *J. Power Sources* **196**, 2433–2444 (2011).
9. E. Antolini, *Energy Environ. Sci.* **2**, 915–931 (2009).
10. M. V. Pagliaro *et al.*, *ACS Catal.* **12**, 10894–10904 (2022).
11. A. Russell, W. S. Epling, *Catal. Rev., Sci. Eng.* **53**, 337–423 (2011).
12. T. Lan *et al.*, *Catal. Sci. Technol.* **10**, 5792–5810 (2020).
13. B. S. Haynes, *Proc. Combust. Inst.* **37**, 1–32 (2019).
14. F. Kuhlmann, "Pour la fabrication de l'acide nitrique et des nitrates," Patent FR11331 France (1838).
15. W. Ostwald, "Improvements in the manufacture of nitric acid and nitrogen oxides." Patent GB190200698A Great Britain (1902).
16. S. Dahl *et al.*, *Phys. Rev. Lett.* **83**, 1814–1817 (1999).
17. J. Neugebohren *et al.*, *Nature* **558**, 280–283 (2018).
18. T. Zambelli, J. Wintterlin, J. Trost, G. Ertl, *Science* **273**, 1688–1690 (1996).
19. C. J. Weststrate, J. W. Niemantsverdriet, *ACS Catal.* **8**, 10826–10835 (2018).
20. M. Zhuo, A. Borgna, M. Saeys, *J. Catal.* **297**, 217–226 (2013).
21. K. Reuter, C. Stampfl, M. V. Ganduglia-Pirovano, M. Scheffler, *Chem. Phys. Lett.* **352**, 311–317 (2002).
22. K. Reuter, M. Scheffler, *Phys. Rev. B Condens. Matter Mater. Phys.* **73**, 045433 (2006).
23. Y.-G. Wang, D. Mei, V.-A. Glezakou, J. Li, R. Rousseau, *Nat. Commun.* **6**, 6511 (2015).
24. Z. Zhang, B. Zandkarimi, A. N. Alexandrova, *Acc. Chem. Res.* **53**, 447–458 (2020).
25. T. Zambelli, J. V. Barth, J. Wintterlin, G. Ertl, *Nature* **390**, 495–497 (1997).
26. J. Neugebohren *et al.*, *Nature* **558**, 280–283 (2018).
27. G. B. Park *et al.*, *Nat. Rev. Chem.* **3**, 723–732 (2019).
28. I. Langmuir, *J. Am. Chem. Soc.* **34**, 1310–1325 (1912).
29. I. Langmuir, *J. Am. Chem. Soc.* **35**, 105–127 (1913).
30. I. Langmuir, *Trans. Faraday Soc.* **17**, 621 (1922).
31. T. Engel, H. Kuipers, *Surf. Sci.* **90**, 181–196 (1979).
32. T. Mitsui, M. K. Rose, E. Fomin, D. F. Ogletree, M. Salmeron, *J. Chem. Phys.* **117**, 5855–5858 (2002).
33. J. Fogelberg, L. G. Petersson, *Surf. Sci.* **350**, 91–102 (1996).
34. M. Jørgensen, H. Grönbeck, *ACS Catal.* **6**, 6730–6738 (2016).
35. D. C. Ford, A. U. Nilekar, Y. Xu, M. Mavrikakis, *Surf. Sci.* **604**, 1565–1575 (2010).
36. M. J. Kratzer, J. Stettner, A. Winkler, *J. Phys. Chem. C Nanomater. Interfaces* **111**, 12723–12729 (2007).
37. R. Westerström *et al.*, *Phys. Rev. B Condens. Matter Mater. Phys.* **76**, 155410 (2007).
38. F. Li *et al.*, *Surf. Sci.* **604**, 1813–1819 (2010).
39. C. T. Campbell, *Top. Catal.* **1**, 353–366 (1994).
40. C. T. Campbell, *ACS Catal.* **7**, 2770–2779 (2017).
41. S. Mallikarjun Sharada, T. Bligaard, A. C. Luntz, G.-J. Kroes, J. K. Nørskov, *J. Phys. Chem. C Nanomater. Interfaces* **121**, 19807–19815 (2017).
42. M. I. Stefan, N. Le Novère, *PLOS Comput. Biol.* **9**, e1003106 (2013).
43. Q. Cui, M. Karplus, *Protein Sci.* **17**, 1295–1307 (2008).
44. C. Bohr, K. Hasselbalch, A. Krogh, *Skand. Arch. Physiol.* **16**, 402–412 (1904).
45. Y. Zhang, K. Reuter, *Chem. Phys. Lett.* **465**, 303–306 (2008).
46. M. Schwarzer, DFT Structures and Kinetic Trace Experimental Data, Dryad (2024); https://doi.org/10.5061/dryad.x3ffbg7vb

SUPPLEMENTARY MATERIALS

science.org/doi/10.1126/science.adk1334
Materials and Methods
Supplementary Text
Figs. S1 to S18
Tables S1 to S15
References (47–60)